Modelling kinetic electron emission for the impact of slow N + on LiF

7 AUTHORS, INCLUDING:

Gerhard Betz
TU Wien
202 PUBLICATIONS **2,305** CITATIONS

SEE PROFILE

Wolfgang Werner
TU Wien
149 PUBLICATIONS **2,723** CITATIONS

SEE PROFILE

Burkhard Fricke
Universität Kassel
303 PUBLICATIONS **3,328** CITATIONS

SEE PROFILE

Modelling kinetic electron emission for the impact of slow N$^+$ on LiF

S. Zamini [a], G. Betz [a], W. Werner [a], F. Aumayr [a], H. Winter [a,*], J. Anton [b], B. Fricke [b]

[a] *Institut für Allgemeine Physik, Technische Universität Wien, Wiedner Hauptstrasse 8–10, A-1040 Vienna, Austria*
[b] *Fachbereich Physik, Universität Kassel, Kassel, Germany*

Abstract

Measured total yields for kinetic electron emission (KE) from the impact of N$^+$ ions on clean polycrystalline LiF at impact energies from the KE threshold up to 5 keV have been modelled with the MARLOWE code for projectile transport in monocrystalline LiF. Electron promotion into the continuum in binary collisions of neutralized projectiles with F$^-$ target anions was regarded as the principal source of slow electron production in the target bulk. With a simple transport model for these slow electrons, we have calculated total electron yields that are typically a factor of five smaller than the respective experimental data. This discrepancy can probably be removed by regarding additional electron production due to recoiling F$^-$ anions and different electron escape conditions for mono- and polycrystalline LiF. © 1998 Elsevier Science B.V. All rights reserved.

Keywords: Ion–solid interactions; Secondary electron emission

1. Introduction

Slow-ion induced electron emission is a ubiquitous phenomenon with important applications, for example, in plasma–wall interactions in gas discharges and experimental thermonuclear fusion devices, or for single-particle detection schemes. According to common distinctions, the collision of an ion with a solid surface gives rise to potential- and/or kinetic electron emission. Potential emission (PE) results from Auger electron transitions driven by internal projectile energy [1,2]. PE requires no kinetic ion energy for it to occur, and it gives rise to total electron yields that strongly increase with the projectile charge, q. At impact energies below 1 a.u. (25 keV amu^{-1}), PE proceeds predominantly above and at the target surface and therefore depends on the target surface-density-of-states (S-DOS) and thus critically on the surface cleanness. Kinetic electron emission (KE), however, proceeds by transferring kinetic projectile energy on to conduction-, valence- and innershell target electrons [3–5] at and below the surface. The resulting KE yields depend primarily on the kinetic projectile energy and, especially at low impact energy, on surface cleanness and the particular combination of involved projectile and target species. For clean metal surfaces, ion-induced electron emission can be satisfactorily described with relatively simple models for PE and KE [1–5], and at low impact energy, the contributions from PE and KE can be regarded as mutually independent and thus additive. For insulator sur-

* Corresponding author. Fax: +43 1 5864203; +43 1 58801-13499; e-mail: winter@iap.tuwien.ac.at

faces, however, the much smaller amount of reliable experimental data is also less well understood. In particular, alkali halides with their pure ionic structure and comparably large band gap provide interesting model surfaces for studying slow ion-induced electron emission from insulators. Respective electron yield measurements are only reliable if surface charge-up by primary and secondary charged species is avoided [6–12]. A comparison of KE from clean LiF- and Au target surfaces for the insulator shows a much lower emission threshold and a total electron yield that increases more rapidly with projectile energy up to higher maximum yields [3–5,11,12]. It has also been observed that for given projectile species and impact energy, the total electron yield from alkali halide surfaces can become smaller with a higher projectile charge, q [10–12], despite an increase of the related PE contribution.

This remarkable behaviour reflects the fact that in alkali halide crystals, the initial projectile charge survives somewhat longer than in metals where strong projectile screening by the quasi-free electron gas takes place. Because, in alkali halides, the principal source of KE results from electron promotion into the continuum in collisions of projectiles with target anions, higher charged projectiles will produce somewhat less KE [13].

In this paper, we describe modelling of total KE yields that have been measured for the impact of slow N^+ ($0.5 \leq E \leq 5$ keV) on polycrystalline LiF [11,12], where the electron yield rises strongly with impact energy, E. Fig. 1 shows the respective data for a polycrystalline LiF target together with similar data for Ar^+ impact [11,12], since only the latter can be compared with earlier measurements that have been carried out for monocrystalline target surfaces. The measurements by Krebs et al. [7,8] were performed with a carefully cleaned LiF(001) surface under UHV conditions (background pressure some 10^{-8} Pa), whereas Arifov et al. [6] worked at a considerably higher background pressure (typically 10^{-3} Pa) and did not specify their target crystal orientation. Both groups obtained total electron yields from ion- and electron current measurements, by keeping the target at about 350°C in order to avoid any surface charge-up. However, in Refs. [11,12], total
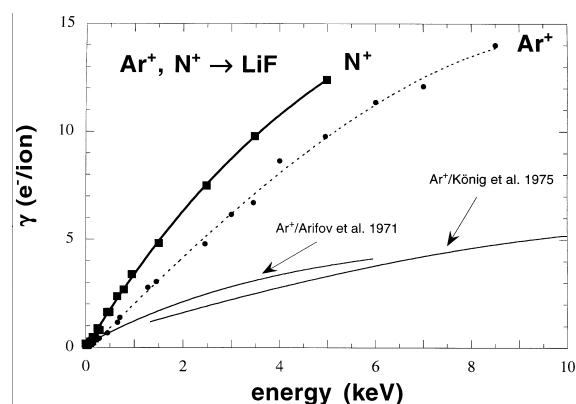

Fig. 1. Measured total electron yields for the impact of N^+ (squares) and Ar^+ (dots) on polycrystalline LiF [11,12], and for the impact of Ar^+ on monocrystalline LiF [6–8], respectively.

electron yields were derived from related electron number statistics by keeping the polycrystalline target at room temperature. Fig. 1 demonstrates a difference by typically a factor of two between electron yields for the Ar^+ impact on polycrystalline and monocrystalline target surfaces, respectively. This discrepancy can be understood from different conditions for electron escape from the target bulk, as will be discussed further in Section 5. A similar difference is expected for bombardment by N^+, for which no other experimental data are available.

Recently, also slow electron energy distributions have been measured for grazing incidence of protons (0.05–1 keV) on a polycrystalline LiF film [14]. These energy distributions could be successfully reproduced by model calculations under the assumption that the principal electron source is electron promotion in H^0–F^- collisions in the target surface layer.

In the present work, modelling of total electron yields has been performed in the following three-stage approach. Stage A, described in Section 2, covers the transport of projectiles inside monocrystalline LiF by means of the simulation code MARLOWE [15]. This code delivers for binary collisions of neutral N^0 with F^- ions within the LiF bulk the collision trajectories near the distances of closest approach together with the respective kinetic energies, from where the main

contribution to slow electron production is expected. In stage B, described in Section 3, the distributed electron source inside the LiF bulk is obtained from electron promotion into the continuum in N^0–F^- collisional quasi-molecules. We assume that projectiles are neutralized soon after surface impact since, in the regarded impact velocity range, their equilibrium charge in the LiF bulk is practically zero. In stage C, which will be described in Section 4, we consider the transport of slow electrons from the LiF bulk across the surface–vacuum barrier, in order to derive the respective total electron yield. The calculated total electron yields turn out to be typically a factor of five smaller than the experimental data from Refs. [11,12]. However, a better agreement within a factor of two or even less can probably be achieved by also taking into account electron production from recoiling anions in the target bulk as well as the polycrystallinity of the LiF target, which has been used in Refs. [11,12].

2. Simulation of projectile transport in the LiF bulk

2.1. Formalism

The first stage in the simulation of KE yields regards collision parameters between impinging particles and target atoms during the slowing down process of the primary particles. To this goal, we have applied the simulation code MARLOWE [15], which is based on the binary collision approximation. The code follows a projectile with a user-defined energy, position and direction, and continues simulating its inelastic binary atomic collisions with the target atoms. This is carried on until the primary particle loses its energy down to below a certain cut-off energy in collisions with the target atoms, or the scattered projectile leaves the target, in other words, it becomes reflected.

After this, MARLOWE will begin the simulation of the next primary particle. The program treats inelastic atomic collisions as a sum of a quasi-elastic part and a separate electronic excitation part. This is possible because the small mass of the electron prevents it from carrying a significant momentum, and the inelastic energy loss in individual collisions is small. In the code, particles are assumed to move only along straight line segments, with these segments being the asymptotes of their paths in the laboratory system. Starting from the equation of motion for the interacting particles trajectories, the respective scattering angles, θ, and time integrals, τ

$$\theta = \pi - 2p \int_R^\infty [r^2 g(r)]^{-1} dr \qquad (1)$$

$$\tau = (R^2 - p^2)^{1/2} - \int_R^\infty \{[g(r)]^{-1} - (1 - p^2/r^2)^{1/2}\} dr, \qquad (2)$$

can be obtained, where p is the impact parameter, and $g(r)$ is defined as follows:

$$g(r) = \left[1 - \frac{p^2}{r^2} - \frac{V(r)}{E_r} \right]^{1/2}. \qquad (3)$$

Furthermore, r is the interatomic separation, $V(r)$ is the potential of the interatomic central force, R is the apsis of the collision defined by $g(R) = 0$ and E_r is the relative kinetic energy:

$$E_r = \frac{M_2 E_0}{M_2 + M_1}, \qquad (4)$$

where M_1 and M_2 are the masses of primary particles and target atoms, respectively, and E_0 is the projectile's initial energy. MARLOWE evaluates the scattering angle and time integrals by using the four-point Gauss–Mehler quadrature.

2.2. Interatomic potentials and inelastic energy loss

Three different screened Coulomb potentials can be applied to the MARLOWE code to simulate the particles interactions, namely the Moliere [16], the Born-Mayer [17] and the Ziegler–Biersack–Littmark potential [18].

Because of the way in which MARLOWE determines the apsis in a collision only, purely repulsive potentials can be used. In our simulations, we have used the Moliere approximation to the Thomas–Fermi screened Coulomb potential as

follows:

$$V(r) = \frac{Z_1 Z_2 e^2}{r} \varphi(r/a), \qquad (5)$$

where

$$\varphi(x) = 0.35 e^{-0.3x} + 0.55 e^{-1.2x} + 0.10 e^{-6x}, \qquad (6)$$

and a is the Firsov screening length:

$$a = \left(\frac{9\pi^2}{128}\right)^{1/3} a_0 (Z_1^{1/2} + Z_2^{1/2})^{-2/3}, \qquad (7)$$

with $a_0 = 0.529$ Å the Bohr radius and Z_1 and Z_2 the atomic numbers of primary particles and target atoms, respectively. The exponential terms in the Moliere potential have the property that the second and third exponential terms are powers of the first one.

At ion velocities significantly less than the Bohr velocity ($v_B = e^2/\hbar$) of the atomic electrons where the energy is less than $1/2 M_1 v_B^2 Z_1^{4/3}$ (M_1 and Z_1 are the atomic mass and number of projectiles, respectively), elastic collisions with target nuclei will dominate.

In the low-velocity regime, i.e. our case of interest, inelastic energy losses can be due to excitation or ionization in both colliding atoms. Since this happens in the electronic shells of atoms, it is called local energy loss. Another possibility that is referred to as a continuous or non-local energy loss is due to the electron gas in a solid (metal); energy is lost continuously along the trajectory of an atom in the solid. The amount of, and the division into, local and non-local energy losses are not well understood at these low bombarding energies, especially for an ionic crystal such as LiF [19,20]. However, the amount of inelastic energy loss is not directly used to evaluate the number of produced electrons. Inelastic energy losses will just reduce the number of collisions of the primary ion as it will lose energy at a higher rate.

At an impact energy of 500 eV, inelastic energy losses, including local and non-local contributions, amount to only about 2% of the primary ion energy and therefore have no influence at all on the number of collisions. At an impact energy of 5000 eV, the dominant contribution is from local energy losses and amounts to about 20% of the incoming projectile energy [21]. An additional inclusion of continuous energy losses would cause a reduction in the number of collisions by about 10%, which is well within the uncertainties of the exact amount of inelastic energy losses in LiF. Therefore, in our simulations, we have used both the local inelastic energy loss of Oen and Robinson [22] and the non-local inelastic energy loss of Lindhard and Scharff [23], with both inelastic energy losses having been described in Ref. [19].

2.3. Results of projectile transport calculations

In the present study, the MARLOWE code was applied for a total of 5000 N projectiles impinging perpendicularly on a LiF target surface with impact energies of 0.5, 1, 3 and 5 keV, respectively. For each projectile trajectory, the model crystal was rotated in a random way to simulate the polycrystalline target structure. The initial impact positions were selected uniformly in a sufficiently large initial impact parallelogram. In the calculation, we have assigned 25 eV to the cut-off energy, below which primary particles were not followed further (see above). Target atom displacements and simultaneous collisions were not allowed in our calculations, and the target was considered to be infinitely thick with one front surface. Our simulation program MARLOWE considered all particles as quasi-neutral.

To study KE, we were only interested in N^0–F^- collisions, and therefore, the energy of the primary particle before each collision, its depth and the respective impact parameter were recorded for all such collisions. The average number of collisions that each primary particle undergoes before it comes to rest is 10.5 for particles with initial energy of 500 eV, 18.5 for 1 keV, 54 for 3 keV and 92 for 5 keV, respectively. More than half of this average value belongs to collisions with F^- target ions. The average penetration depth of the N^0 atoms was 13.3, 24.9, 80.8 and 141.6 Å, respectively for the above mentioned impact energies.

Depth distributions of penetrated N^0 atoms in

the LiF bulk are shown in Fig. 2 for initial impact energies of 0.5, 1, 3 and 5 keV, respectively. Fig. 3 shows the impact parameter distributions versus depth below the target surface. At 500 eV, almost all relevant collisions take place within the first 20 Å, and the number of collisions within the first 10 Å is more than twice the value within the second depth bin (i.e. 10–20 Å). With increasing impact energy, the projectiles penetrate deeper, and therefore, the number of electron-producing collisions in greater depths increases accordingly. Although these impact parameter distributions are plotted up to a depth of 130 Å, simulations for N^0 impact at 3 and 5 keV show a significant number of collisions also at greater depths.

3. Calculation of electron production inside the LiF bulk

3.1. Electron production probability in single collisions

The basis of our analysis is the calculation of the impact parameter dependent ionization probability in a N^0–F^- binary collision as a function of impact energy. Details of this formalism can be found in a series of papers [24–26]. We will give here only a brief outline. In such a binary collision
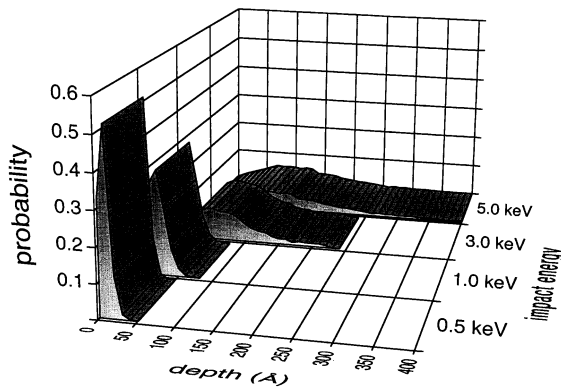

Fig. 2. Penetration depth distributions for 5000 N particles with initial energies of 0.5, 1, 3 and 5 keV, respectively, in a LiF monocrystalline target.

system, the electron motion is described in the semi-classical approximation for the motion of the nuclei by the electronic, time-dependent, many-particle Dirac equation:

$$i\hbar \frac{\partial \Psi(\vec{r}_i, t)}{\partial t} = \hat{H} \Psi(\vec{r}_i, t), \qquad (8)$$

where $\vec{r}_i$ are the electronic coordinates. For the total wave function of the whole system, Ψ, we choose a Slater determinant which is built from time-dependent single-particle wave functions $\psi_i(\vec{r}, t)$. These wave functions, $\psi_i(\vec{r}, t)$, are calculated as the solution of the N molecular Dirac–Fock–Slater (DFS) equations for all N electrons,

$$\left\{ \hat{t} \hat{V}^N[R(t)] + \hat{V}^C[\rho(t)] + \hat{V}_\alpha^{Ex}[\rho(t)] - i\hbar \frac{\partial}{\partial t} \right\}$$
$$\psi_i(\vec{r}, t) = 0, \ i = 1, \dots, N, \qquad (9)$$

where t is the kinetic operator, and the potentials in these equations are the electron–nucleus potential, V^N, the electron–electron Coulomb potential, V^C, and the Slater exchange potential, V^{Ex}.

To solve Eq. (9), we expand the wave functions in terms of static Molecular Orbitals $\phi_j(\vec{r}, R)$

$$\psi_i(\vec{r}, t) = \sum_j^M a_{ji}(t) \phi_j[\vec{r}, R(t)] e^{[-(i/\hbar) \int \epsilon_j(t') \, dt']}. \qquad (10)$$

Inserting this ansatz into Eq. (9), the N DFS equations can be rewritten as a coupled set of differential equations for the amplitudes, $\{a_{ij}\}$, the well-known coupled channel equations

$$\dot{a}_{ij} = \sum_m -a_{mi} \left\langle \phi_j \Big| \frac{\partial}{\partial t} \Big| \phi_m \right\rangle e^{[-(i/\hbar) \int (\epsilon_j - \epsilon_m) \, dt']},$$
$$j = 1, \dots, N. \qquad (11)$$

The dynamic coupling matrix elements:

$$\left\langle \phi_j \Big| \frac{\partial}{\partial t} \Big| \phi_m \right\rangle$$

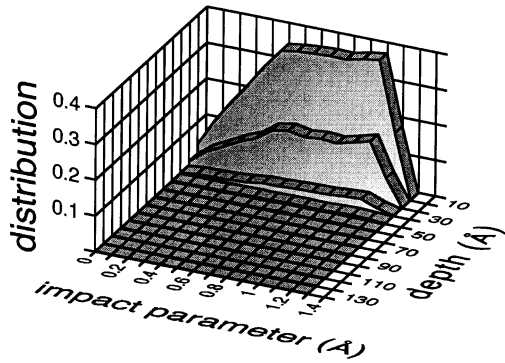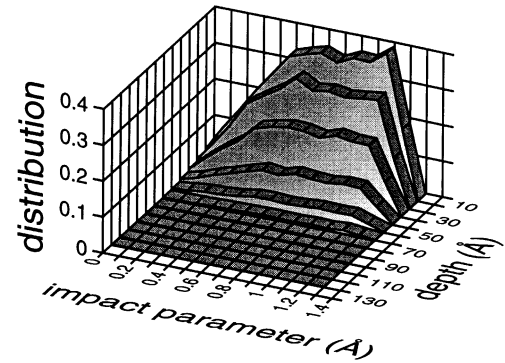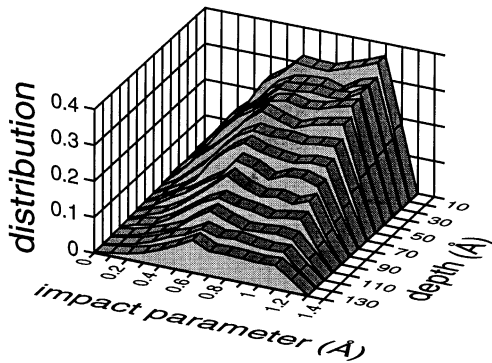can be rewritten in the form of rotational- and radial coupling matrix elements, which we obtain
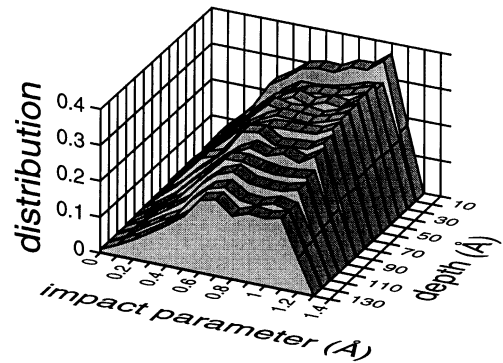
E = 0.5 keV

E = 1.0 keV

E = 3.0 keV

E = 5.0 keV

Fig. 3. Impact parameter distributions vs. depth for 5000 N particles in collisions with F^- atoms on monocrystalline LiF, with initial energies of 0.5, 1, 3 and 5 keV, respectively.

by solving the static DFS equation

$$\{\hat{t} + \hat{V}^N + \hat{V}^C[\rho(\vec{r}, R)] + \hat{V}_\alpha^{Ex}[\rho(\vec{r}, R)]\}$$

$$\times \phi_j(\vec{r}, R) = \epsilon_j \phi_j(\vec{r}, R) \qquad (12)$$

at a large number of internuclear distances, R, by using the MO-LCAO- (Molecular Orbital Linear Combination of Atomic Orbitals) Method. As a basis to solve the DFS Eq. (12), we use an atomic, R-dependent, three-center basis [26], which leads us to an accurate calculation of the eigenvalues and coupling matrix elements at all internuclear distances. After solving the coupled-channels equations, the formalism of inclusive probabilities [27] allows us to calculate many-particle probabilities from the set of single-particle amplitudes $\{a_{ij}\}$.

This is the reconstruction of the realistic many-particle wave function $\Psi(\vec{r}_i, t)$ in Eq. (8). The procedure of an actual calculation is as follows. The correlation diagram for the scattering system N^0–F^- (see Fig. 4) is calculated. In the initial ground state configuration, the lowest $n=1$ and $n=2$ levels of N^0 and F^- (see the right hand side of Fig. 4) are occupied by 18 electrons. We solve the coupled-channels equations along a classical trajectory for several impact parameters and impact energies in a subspace of 42 static MOs, and calculate from the single-particle amplitudes the probability of having at least one electron at any one of the upper states which correlate to the M- and N shells of the colliding particles. These shells have diameters that are similar in size to the
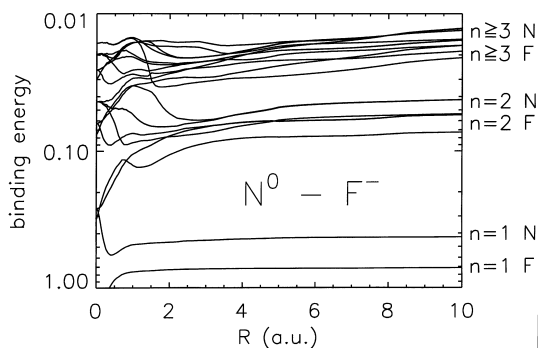
Fig. 4. (N^0–F^-) correlation diagram for calculating the electron production source in the LiF bulk.

LiF lattice spacing (about 2 Å), and therefore, our calculated electron yield (see Fig. 5) is a good approximation for free electron production in the scattering system.

3.2. Electron production in the LiF bulk

The above simulations have been performed for N^0–F^- collisions at impact energies of 0.5, 1, 3 and 5 keV, respectively. The kinetic energy of the incident N^0 projectiles changes after each collision due to elastic and inelastic processes when penetrating the polycrystalline LiF. To take this into account, the data shown in Fig. 5a–d were interpolated to obtain the electron production within the whole impact energy range below 5 keV. Fig. 6 shows the derived total electron production inside the LiF bulk vs. the initial projectile impact energy. Electrons produced in different depths of the LiF bulk are assumed to be slow (≤ 10 eV, cf. Refs. [7,8,14]). Fig. 7 shows how, with higher impact energy, the number of electrons in deeper layers increases accordingly. In contrast to the situation assumed in Ref. [14], we had to take into account the fact that electrons produced farther inside the target bulk are less likely to move from the surface into vacuum, as described below.

4. Transport of slow electrons from the LiF bulk into vacuum

Transport models for low-energy electrons in a solid have to be based on detailed knowledge

about the electronic structure of the target material that determines the excitation mechanisms influencing electron scattering. Unfortunately, this complicates modelling of electron transport in alkali halides since literature data on their band structure are contradictory. For example, in an important survey, Poole et al. [28] quote theoretical electron affinities, χ, ranging from -6.1 to $+5.4$ eV. Here, the electron affinity is defined as the energy difference between the bottom of the conduction band and the vacuum level [29]. Even if the exact band structure of a solid were unambiguously established, the effective band structure of the real solid can be quite different because the latter possibly contains defects and may also be perturbed by projectile-induced collision cascades, which makes the basis of such model calculations still less secure. Some models [30–34] assume that the electron affinity is small (of the order of 1 eV) and positive. However, band structure calculations by Kunz [35] for LiF predict a negative electron affinity of about -2 eV.

In any case, for electrons with kinetic energies less than the band gap, inelastic interactions are precluded, and the absorption will then be dominated by phonon losses. To tackle the problems addressed above, we have performed calculations for two cases, which are illustrated in Fig. 8. The left hand side of Fig. 8 corresponds to a case with positive electron affinity, referred to as model I. For kinetic electron energies below E_g, absorption will be dominated by phonon losses (see above). The contrasting case depicted on the right hand side of Fig. 8, referred to as model II, follows Ref. [35] in assuming that the vacuum level is located within the band gap (negative electron affinity). Here, we make the additional assumption that electronic states are available in sufficient density just below the vacuum level in the gap and are attributable to bulk- and surface exciton states [36]. In this case, electronic excitation is allowed within the upper part of the band gap and will then dominate the transport behaviour, since the related stopping power for electrons is much higher than for phonon scattering where transferred energies can be of the order of kT only. Both electronic (i.e. inelastic) and phonon scattering losses are considered in model II. In both models, we essen-
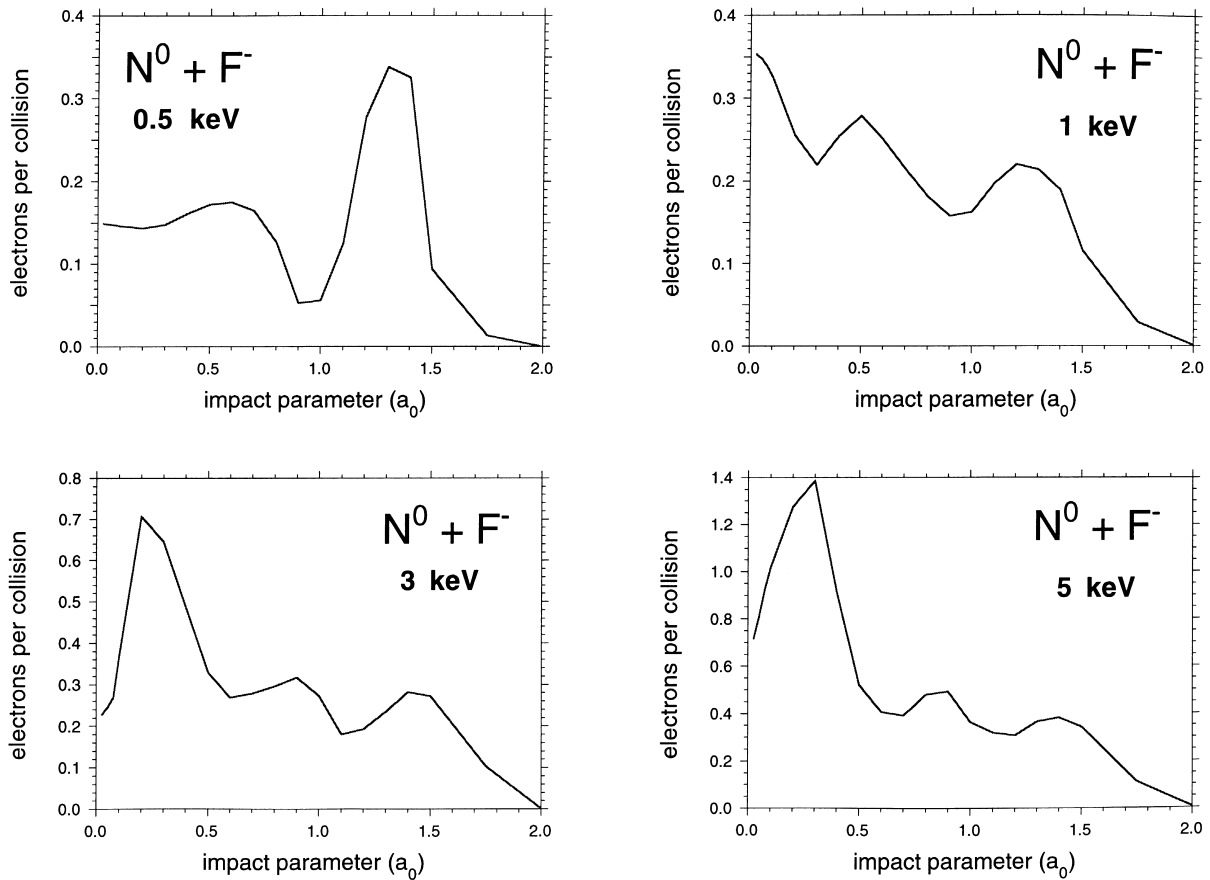
Fig. 5. Number of electrons emitted in single N^0–F^- collisions as a function of impact parameter, at initial projectile energy of 0.5, 1, 3 and 5 keV, respectively.

tially take into account the following four processes for the transport of slow electrons:

(1) deflections in elastic interactions with the screened Coulomb potential of target nuclei;
(2) deflections associated with momentum transfer in inelastic events;
(3) energy losses due to excitation of LiF valence electrons or phonons; and
(4) escape over the surface barrier.

Qualitatively, the slow electron transport may be understood by realizing that the characteristic length for absorption (i.e. the distance measured along the trajectory until the electron energy becomes too low for escape) greatly exceeds the characteristic length for large angle deflections. This corresponds to intensive scattering or rapid

momentum relaxation and allows the transport approximation to be applied to describe the deflection term in the kinetic equations [37,38]. In this transport approximation, the deflection function is isotropic, whereas the rate of scattering is determined by the cross-section for momentum transfer $\sigma_{tr} = (N_a \lambda_{tr})^{-1}$, where N_a is the atomic density, and λ_{tr} is the transport mean free path.

To account for deflections in elastic as well as inelastic collisions, the corresponding transport mean free paths were calculated by using the relation

$$\frac{1}{\lambda_{tr}^{tot}(E)} = \frac{1}{\lambda_{tr}^{i}(E)} + \frac{1}{\lambda_{tr}^{e}(E)}. \qquad (13)$$

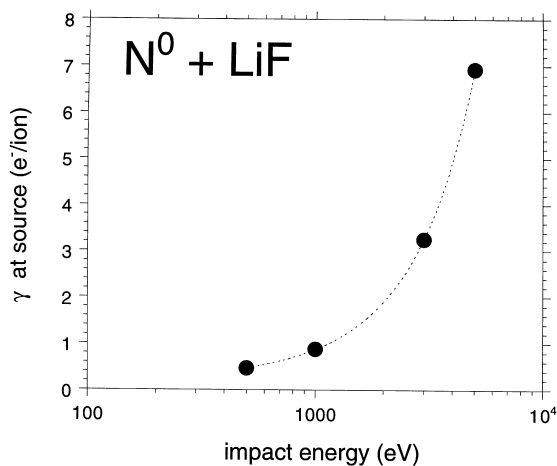Here, the superscripts i and e refer to inelastic and

Fig. 6. Number of electrons produced per primary ion inside the LiF bulk, vs. initial impact energy.
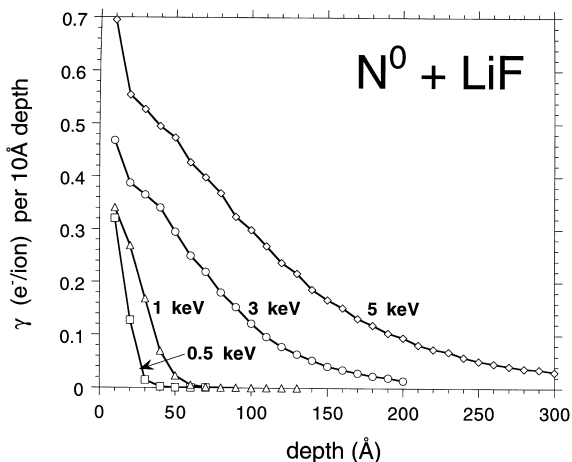

Fig. 7. Number of electrons produced per impact inside the LiF bulk within depth layers with thicknesses of 10 Å, for N^0–F^- collisions with different impact energies.

elastic collisions, respectively, and E denotes the actual electron energy at a certain point along the trajectory. The inelastic transport mean free path was estimated by applying Penn's algorithm [39] to optical data in Ref. [40]. The same procedure was followed to establish values for the inelastic mean free path. The phase shifts needed to evaluate the elastic transport mean free path were obtained with the relativistic code by Yates [41] using a Thomas–Fermi–Dirac potential [42] for free atoms. The transport cross-section for LiF was
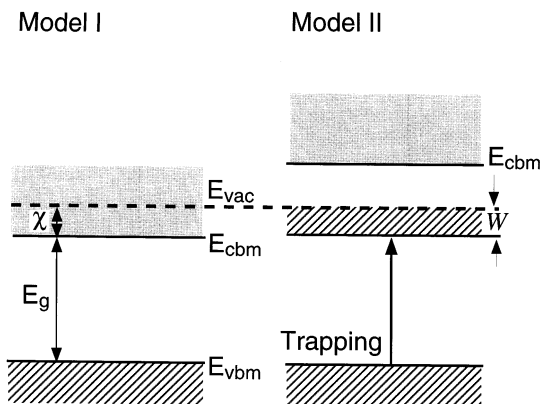

Fig. 8. Illustration of two alternative model electronic structures for LiF used in the slow electron transport calculations. In model I (left side), it is assumed in accordance with Refs. [30–34] that the electron affinity is positive and phonon losses dominate the inelastic interaction. In model II (right side), it is supposed that within the band gap ($E_g = 14$ eV, $E_{vac} - E_{vbm} = 10$ eV; [35]), there exists a band W of allowed energies which is available for absorption of electrons via electronic excitation. Absorption is assumed to be possible only for energy losses within the range $(E_{vac} - W - E_{vbm}) < (E_{vac} - E_{vbm})$. Inelastic energy losses are supposed to promote electrons from the valence band maximum into defect band W of localized states ("Trapping").

calculated by averaging elastic scattering cross-sections for Li and F, and using these results for calculating the mean free path as explained in Refs. [37,38]. The inelastic mean free paths and energy transfer for phonon losses were taken from the work of Llacer and Garwin [43]. The classical transmission coefficient was applied to describe escape over the surface barrier, i.e. only electrons arriving at the surface with a polar direction smaller than the critical angle $\theta_c = \arccos(U_o/E)^{1/2}$ can be transmitted while all others are (specularly) reflected. Here, U_o is the barrier height that is commonly taken to be equal to the electron affinity. Having determined the interaction parameters in the way described above, the kinetic equations were solved by employing a Monte Carlo technique and using the results of the MARLOWE simulations from Sections 2 and 3 for the depth distribution of the slow electron sources.

The angular distribution was taken to be isotropic, whereas the source energy distribution was assumed to decay exponentially above the vacuum

level with a decay energy of 10 eV, as is characteristic for measured energy distributions of emitted electrons [7,8,14].

In model II, the band width, W, of allowed states within the band gap (cf. Fig. 8, right hand side) was used as a free parameter in our calculations. If a given energy loss leads to a transition of slow electrons into this "band", such electrons are assumed to be absorbed and their trajectories regarded as terminated. The energy thereby transferred is supposed to be absorbed by an electron from the top of the valence band, which will be excited into region W.

5. Comparison of modelled and experimental electron yields

By following the procedures described in Sections 2–4, we have calculated total electron yields for impact of N^+ on monocrystalline lithium fluoride for ion impact energies of 0.5, 1, 3 and 5 keV respectively. Slow electron transport from the LiF bulk into vacuum has been treated alternatively with models I and II as described in Section 4.

The calculated yields are compared with corresponding experimental data for polycrystalline LiF from Refs. [11,12] in Fig. 9a (electron transport treated with model I) and Fig. 9b (electron transport treated with model II), respectively. Regarding the impact energy dependence, both sets of calculations are in satisfactory agreement with the experimental data. With respect to absolute yield values, however, there is a large disagreement between the experimental and modelled yields, with the latter being too low by, typically, a factor of five, if electron transport model II is applied. We believe that the electron transport model II is more appropriate than model I, since the existence of surface and bulk exciton states within the LiF band gap has been experimentally demonstrated (cf. [36] and references therein).

We propose two reasons for the apparent discrepancy in absolute yields:
(1) Measured KE yields from Ref. [11,12] have been obtained with a polycrystalline LiF film target with random orientation of the target
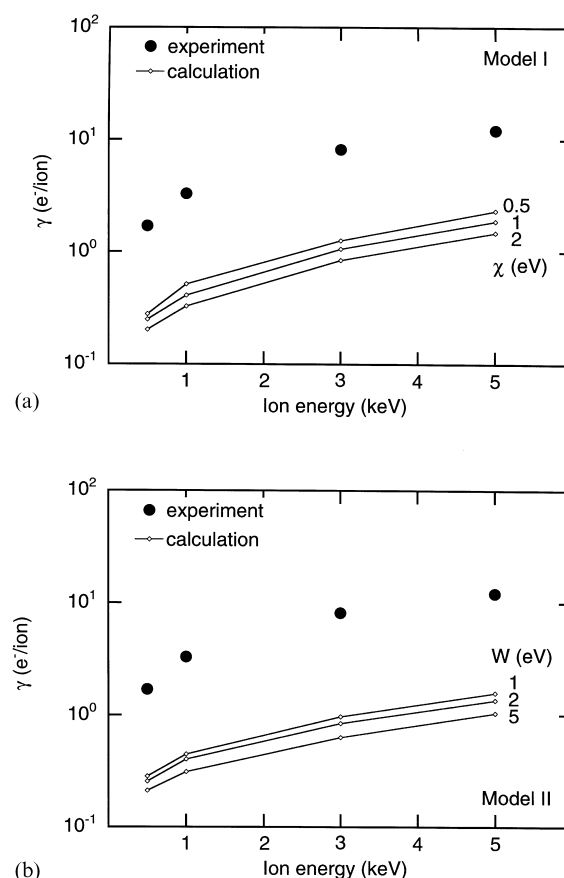

Fig. 9. (a) Comparison of calculated (this work, monocrystalline LiF, application of slow electron transport model I) and measured total electron yields (polycrystalline LiF [11,12]) for the impact of N^+ on LiF. (b) Comparison of calculated (this work, monocrystalline LiF, application of slow electron transport model II) and measured total electron yields (polycrystalline LiF, [11,12]), for the impact of N^+ on LiF.

crystallites, for which considerably higher total electron yields can be expected than for a monocrystalline LiF target. This is well supported by a comparison of total electron yields measured for impact of Ar^+ on similar polycrystalline LiF films [11,12] with two sets of measurements involving clean LiF monocrystalline surfaces [6–8] (cf. Fig. 1). For polycrystalline LiF, the KE yield is about twice as large as that for moncrystalline LiF. This difference is understood from the fact that for randomly oriented LiF crystallites, consider-

ably more electron-producing collisions take place in the near-surface region from where electrons can easily escape into the vacuum [1–5].

(2) For our calculated electron source in the LiF bulk, neither projectile collisions with Li^+ kations nor F^- recoil collisions with F^- or Li^+ target constituents have been taken into account.

According to some preliminary calculations, incorporation of these additional electron-producing mechanisms into the transport calculations, as described in this work, should increase the calculated total KE yields by about a factor of two. Together with the influence of the polycrystalline target structure (see above), this should lead to agreement of our modelled KE yields with the experimental data from Refs. [11,12] within a factor of two or even less, which, in view of the comparably simple approach of our model calculations, can be regarded as satisfactory.

As a principally different access to the electron production source term, we may treat the interaction of a nitrogen projectile with the LiF target bulk so as to lead to a temporary bandgap reduction in the latter. In this way, Eder et al. [44] calculated the stopping power of slow protons in thin LiF films. The temporary presence of a neutralized proton in the LiF crystal lattice causes a local reduction of the LiF bandgap by more than a factor of three, which greatly enhances the probability for electron promotion from the HOMO (highest occupied molecular orbital) into the LUMO (lowest unoccupied molecular orbital) of the LiF crystal. So far, however, this other possible way of calculating the electron source function in the LiF bulk has not been further pursued.

6. Summary and conclusions

We have performed model calculations of total kinetic electron (KE) emission yields from polycrystalline LiF bombarded by slow N^+ ions at impact energies from 0.5 to 5 keV. With respect to impact energy dependence, our calculations reproduce the available experimental data reason-

ably well. The remaining large discrepancy in the size of total electron yields by typically a factor of five can probably be satisfactorily removed if we take account of the principal difference for KE from polycrystalline and monocrystalline LiF surfaces and, furthermore, of additional electron production in collisions of N^+ with Li^+ as well as of recoiling F^- with LiF constituents, which "secondary processes" have not been incorporated in the present calculations. We believe that such extended modelling calculations will probably cover most of the relevant processes for kinetic electron emission, i.e. projectile transport, slow electron production inside the LiF bulk and attenuation of slow electrons on their way from the target bulk across the vacuum barrier. For more detailed modelling, we would require more systematic measurements of KE yields for impact of various projectile ions on mono- and polycrystalline LiF- and other alkali halide target surfaces.

References

[1] P. Varga, HP. Winter, in: Particle Induced Electron Emission II, Springer Tracts in Modern Physics 123, Springer, Berlin, 1992.

[2] R. Baragiola, in: J.W. Rabalais (Ed.), Low Energy Ion–Surface Interaction, Chap. 4, Wiley, New York, 1994.

[3] J. Schou, Scanning Microsc. 2 (1988) 607.

[4] M. Rösler, W. Brauer, in: G. Höhlek (Ed.), Particle Induced Electron Emission I, Springer Tracts in Modern Physics 122, Springer, Berlin, 1991.

[5] D. Hasselkamp, in: G. Höhlek (Ed.), Particle Induced Electron Emission II, Springer Tracts in Modern Physics 123, Springer, Berlin, 1992.

[6] U.A. Arifov, R.R. Rakhimov, S. Gaipov, Izv. Akad. Nauk SSR Ser. Fiz. 35 (1971) 562.

[7] W. König, H.H. Krebs, S. Rogaschewski, Int. J. Mass Spectrom. Ion Phys. 16 (1975) 243.

[8] K.H. Krebs, S. Rogaschewski, Wiss. Z. Humboldt-Univ. Berlin, Math.-Nat. R. XXV (1976) 3.

[9] S.S. Radzhabov, R.R. Rakhimov, D. Abdusalamov, Izv. Akad. Nauk SSSR Ser. Fiz. 40 (1976) 2543.

[10] S.N. Morozov, D.D. Gruich, T.U. Arifov, Izv. Akad. Nauk SSSR Ser. Fiz. 43 (1979) 612.

[11] M. Vana, F. Aumayr, P. Varga, HP. Winter, Europhys. Lett. 29 (1995) 55.

[12] M. Vana, F. Aumayr, P. Varga, HP. Winter, Nucl. Instrum. Meth. Phys. Res. B 100 (1995) 284.

[13] L.M. Kishinevskii, E.S. Parilis, Sov. Phys. Tech. Phys. 27 (1982) 784.

[14] P. Stracke, F. Wiegershaus, S. Krischok, V. Kempter, P.A. Zeijlmans van Emmichoven, A. Niehaus, F.J. Garcia de Abajo, Nucl. Instrum. Meth. Phys. Res. B 125 (1997) 67.

[15] M.T. Robinson, in: MARLOWE (Version 13) User's Guide, Solid State Div., Oak Ridge National Laboratory, Oak Ridge, 1992.

[16] G. Moliere, Z. Naturforsch. A 2 (1947) 133.

[17] H.H. Anderson, P. Sigmund, Nucl. Instrum. Meth. 38 (1965) 238.

[18] J.F. Ziegler, J.P. Biersack, U. Littmark, US Department of Energy Report ORNL/CONF-82013, 1983, p. 88.

[19] W. Eckstein, Computer Simulation of Ion–Solid Interactions, Springer Series in Materials Science 10, Springer, Berlin, 1991

[20] M.T. Robinson, J. Nucl. Mater. 216 (1994) 1.

[21] S. Zamini, Ph.D. thesis, TU Wien, in preparation.

[22] O.S. Oen, M.T. Robinson, Nucl. Instrum. Meth. 132 (1976) 647.

[23] J. Lindhard, M. Scharff, Phys. Rev. 124 (1961) 128.

[24] W.-D. Sepp, D. Kolb, W. Sengler, H. Hartung, B. Fricke, Phys. Rev. A 33 (1986) 3679.

[25] P. Kürpick, W.-D. Sepp, B. Fricke, Phys. Rev. A 51 (1995) 3693.

[26] J. Anton, K. Schulze, P. Kürpick, W.-D. Sepp, B. Fricke, Hyperfine Interac. 108 (1997) 89–94.

[27] P. Kürpick, H.-J. Lüdde, Comp. Phys. Comm. 75 (1993) 127.

[28] R.T. Poole, J. Liesegang, R.C.G. Leckey, J.G. Jenkin, Phys. Rev. B 11 (1975) 5190.

[29] H. Ibach, H. Lüth, Solid State Physics, Springer, Berlin, 2nd ed., p. 363.

[30] R.T. Poole, J. Liesegang, R.C.G. Leckey, J.G. Jenkin, Phys. Rev. B 11 (1975) 5179.

[31] B.L. Henke, J. Liesegang, S.D. Smith, Phys. Rev. B 19 (1979) 3004.

[32] J. Schou, in: Physical Processes of the Interaction of Fusion Plasmas with Solids, Academic Press, London, 1996, p. 177

[33] J. Schou, Scanning Microsc. 2 (1988) 607.

[34] A. Akkerman, A. Breskin, R. Chechik, A. Gibrekhterman, in: R.A. Baragiola (Ed.), Ionization of Solids by Heavy Particles, Plenum Press, New York, 1993, p. 359.

[35] A.B. Kunz, Phys. Rev. B 26 (1982) 2056.

[36] P. Wurz, J. Sarnthein, W. Husinsky, G. Betz, P. Nordlander, Y. Wang, Phys. Rev. B 43 (1991) 6729.

[37] I.S. Tilinin, Sov. Phys. JETP 55 (1982) 751.

[38] I.S. Tilinin, W.S.M. Werner, Mikrochim. Act. 114/115 (1994) 485.

[39] D.R. Penn, Phys. Rev. B 35 (1985) 482.

[40] E.D. Palik, Handbook of Optical Constants of Solids, Academic Press, New York, 1985.

[41] A.C. Yates, Comp. Phys. Comm. 2 (1971) 175.

[42] R.A. Bonham, T.G. Strand, J. Chem. Phys. 39 (1963) 2200.

[43] J. Llacer, E.L. Garwin, Phys. Rev. B 40 (1969) 2766.

[44] K. Eder et al., Phys. Rev. Lett. 79 (1997) 4112.